

Coseismic slip distributions of the 26 December
2004 Sumatra-Andaman and 28 March 2005 Nias
earthquakes from GPS static offsets

July 10, 2006

Paramesh Banerjee¹, Fred Pollitz², B Nagarajan³, and Roland Bürgmann⁴

¹*Wadia Institute of Himalayan Geology, Dehra Dun, India;* ²*USGS, Menlo Park, CA, USA;* ³*Geodetic and Research Branch, Survey of India, Dehra Dun, India;* ⁴*Dept. Earth and Planetary Sci., UC Berkeley, CA, USA.*

Abstract

Static offsets produced by the 26 December 2004 M_w 9 Sumatra-Andaman earthquake as measured by GPS reveal a large amount of slip along the entire $\gtrsim 1300$ km-long rupture. Most seismic slip inversions place little slip on the Andaman segment, whereas both near-field and far-field GPS offsets demand large slip on the Andaman segment. We compile available datasets of the static offset in order to render a more detailed picture of the static slip distribution. We construct geodetic offsets such that post-earthquake positions of continuous GPS sites are

reckoned to a time 1 day after the earthquake and campaign GPS sites are similarly corrected for postseismic motions. The newly revised slip distribution ($M_w = 9.22$) reveals substantial segmentation of slip along the Andaman Islands, with the southern quarter slipping ~ 15 m in unison with the adjacent Nicobar and northern Sumatran segments of length ~ 700 km. We infer a small excess of geodetic moment relative to the seismic moment. A similar compilation of GPS offsets from the 28 March 2005 Nias earthquake is well explained with dip slip averaging several meters ($M_w = 8.66$) distributed primarily at depths greater than 20 km.

1 Introduction

The 26 December 2004 $M \sim 9$ Sumatra-Andaman earthquake and 28 March 2005 $M = 8.7$ Nias earthquake ruptured portions of the Sumatra and Sunda subduction zones over lengths of ~ 1500 km and ~ 400 km, respectively (Figure 1). The slip distribution of the Sumatra-Andaman earthquake has been estimated from seismic waves (Ammon et al., 2005; Lay et al., 2005), static offsets (Banerjee et al., 2005; Vigny et al., 2005; Subarya et al., 2006), and joint seismic-geodetic data (Chlieh et al., 2006). The overall size of the earthquake has been further constrained by Earth’s free oscillations (Stein and Okal, 2005; Park et al., 2005). Each study makes use of a different frequency band, and as first noted by Stein and Okal (2005) and subsequent investigators, the apparent earthquake size increases with period. Banerjee et al. (2005) found that the effectively zero-frequency static offsets, based on a combination of preseismic and 0 to 5 day postseismic Global Position-

ing System (GPS) measurements, apparently required an earthquake size of order 30% larger than that detected by long-period free oscillations, independent of the strong correlation of the estimated moment and dip in both seismic and geodetic estimates of magnitude. However, the size of the source required to explain free oscillation measurements increases when a finite source-time function, rather than an impulsive source, is used because of phase cancellation (Park et al., 2005). The free oscillation measurements are well-explained with a source of ~ 600 sec duration over a broad range of frequencies (Park et al., 2005), with a seismic moment of 6.5×10^{22} Nm, the same as that inferred by Banerjee et al. (2005). The excellent fit of a distributed slip model to joint seismic and geodetic datasets (Chlieh et al., 2006) shows directly that the two types of data are essentially compatible and yield the same earthquake size.

The seismic investigations have used large seismic datasets, resulting in detailed slip models of the earthquake at seismic periods up to 1 hour. Investigations based on the static offsets cannot resolve the temporal evolution of slip, but allow a better picture of the net coseismic slip distribution. They are also ideally suited to detect slip at a time scale much greater than the seismically-detected rupture duration. However, previous investigations of the static offset are based on measurements that typically include several days of postseismic motions. The very rapid motions obtained by continuous GPS measurements in the days following the earthquake (e.g. Vigny et al., 2005), when integrated over several days, are generally a substantial fraction of the actual coseismic offset. The purpose of this paper is to expand and revise the 26 December 2004 static-offset dataset of Banerjee et al. (2005) in

order to afford a more detailed picture of the net coseismic slip distribution. Where possible we apply corrections for postseismic offsets in order to render a clearer picture of the coseismic offset. We conduct a similar analysis of static offsets from the 28 March 2005 Nias earthquake in order to derive a simple slip distribution consistent with applicable geodetic data as well as seismotectonic constraints.

2 26 December 2004 Data Set

The GPS datasets of Banerjee et al. (2005) (their Table S1) and Vigny et al. (2005) (their Table 1) consist of horizontal velocity vectors estimated at 41 and 86 continuously operating sites (CGPS), respectively. We have expanded the dataset analyzed by Banerjee et al. (2005) to include 11 more sites belonging to various regional CGPS networks and 11 sites surveyed in campaign-mode (SGPS) before and after the event by the Survey of India (SOI)(Gahalaut et al., 2006). GPS data from the CGPS sites were processed with the GAMIT/GLOBK software package (King and Bock, 2005; Herring, 2005) to produce time series of station coordinates in the ITRF-2000 reference frame. We used 18 global IGS GPS stations to implement the ITRF-2000 reference frame in the GPS analysis. Stations used to define the reference frame are > 4500 km from the earthquake rupture. Time series at continuous GPS site PHKT is shown in Figure 2; time series at several other sites are shown in Figure S1. Coseismic offsets of the CGPS sites are estimated by, first, determining the best-fitting straight lines to 18-day pre-seismic and 9-day postseismic portions of the time series; second, choosing

a time t_0 on the preseismic line segment just prior to the earthquake and a time t_1 on the postseismic line segment just after the earthquake. Red and green line segments in Figure 2 illustrate line-segment fits obtained with the first step in the pre-seismic and post-seismic time intervals, respectively. When fewer than 18 days or 9 days of observations are available during the pre-seismic or post-seismic epochs, respectively, then as many days as possible are used.

Ideally the separation between t_0 and t_1 should be only a few minutes, the duration of the seismically-detected part of the earthquake (e.g. Ammon et al., 2005). However, suggestions of slow slip lasting on the order of one hour (Stein and Okal, 2005; Bilham et al., 2005) or longer (Banerjee et al., 2005) suggest that t_1 be chosen such that the earthquake "duration" $t_1 - t_0$ be somewhat greater than one hour. We find that offsets estimated in this fashion are very similar for durations of $t_1 - t_0 = 1$ day and 2.5 days. The maximum slope of the first 9-days postseismic time series is -1.36 mm/day for the East component of PHKT, corresponding to 2 mm westward movement between postseismic days 1 and 2.5 after the earthquake, and slopes at all other sites are much smaller (Figure S1). Thus we consider a duration of $t_1 - t_0 = 1$ day as a satisfactory choice for capturing essentially all of the coseismic signal without introducing much postseismic signal, which could arise from afterslip, viscoelastic relaxation, etc. The complete set of 53 coseismic horizontal displacement vectors derived in this study from our analysis of CGPS measurements is given in Table S1 and plotted in Figure 3. We append an additional 55 displacement vectors from Vigny et al. (2005), corrected for postseismic displacements as explained in the Supplementary

Online Material. These are presented in Table S2 and are shown by the blue vectors in Figure 3. Together with our newly determined offsets, this comprises a total of 108 far-field GPS static offsets.

The Survey of India (SOI) carried out GPS campaign measurements of 13 survey points on the Andaman and Nicobar Islands in March, 2004, 12 of which were re-surveyed after the 26 December 2004 event (Gahalaut et al., 2006). We have processed these data using the approach described above and estimated their horizontal and vertical offsets (Table S3). (The tabulated offsets include a small correction for postseismic motions as explained below and listed in Table S3.) We appended an additional three-dimensional offset at Car Nicobar supplied by Table 1 of Jade et al. (2005). These offsets are plotted in Figures 4 and 5. The campaign measurements were collected during the time period 10 to 28 days following the earthquake and include 264 to 300 days of interseismic deformation prior to the event. They therefore include the effects of an unknown amount of afterslip and a small amount of pre-earthquake deformation. Subarya et al. (2006) present campaign measurements from northern Sumatra that also span the earthquake and about 1.5 months of postseismic deformation (their supplement tables S1 and S2), which we also include in our analysis.

The question arises as to how much postseismic motions are present in the SGPS measurements from the Andaman Islands and northern Sumatra. Guidance is provided by CGPS measurements. Figure 6 shows estimated postseismic motions from 1 to 50 days after the earthquake at several CGPS sites. This includes postseismic time series at a new CGPS site CAR2 spanning the time period from 25 to 55 days after the earthquake, which

constrains the postseismic motions in its locality near Port Blair (Paul et al., 2005). The extrapolation of this motion to the period 1 to 50 days after the earthquake, using a $\log(t)$ dependence, is about 33 cm towards the WSW (Figure 6). Extrapolated motion to the period 1 to 19 days after the earthquake (the mean epoch when post-earthquake campaign measurements were made in the Andaman Islands) is about 24 cm, about 8% of the coseismic offset at nearby Port Blair. A composite time series derived from two co-located sites PORT and CAR2 (Figure 7), spanning the time interval from 10 to 100 days after the earthquake, confirms these extrapolations. Although this pertains to a restricted area of the Andaman Islands, it suggests that most of the signal in these campaign measurements are the coseismic offset, and little bias is introduced by neglecting any correction for postseismic motions in the Andaman Islands.

Nevertheless, we assess the likely postseismic motions and correct the SGPS measured offsets using a physical model. Both afterslip (e.g. Hashimoto et al., 2006a,b) and asthenosphere relaxation (Pollitz et al., 2005) are equally capable of explaining the observed postseismic motions. Models of both classes can be constructed that well fit the observed horizontal postseismic motions, but the two models generally yield very different patterns of vertical postseismic motions. Within the class of afterslip models, the magnitude and sign of predicted vertical offsets is sensitive to the afterslip fault geometry, particularly the upper edge depths of the afterslip planes. It is difficult to construct an afterslip model uniquely since there is little independent control on possible afterslip geometry apart from the PORT/CAR2 time series. Within the class of postseismic models, the magnitude and sign of

predicted vertical postseismic motions depends on the distribution of slip within the elastic plate, the viscoelastic structure of the asthenosphere, etc. Predicted horizontal postseismic motions from these models are more robust. We thus consider a mechanical model of postseismic motions to be useful for correcting observed horizontal offsets but not observed vertical offsets.

For simplicity we postulate that afterslip is responsible for the observed postseismic motions and construct a dislocation model that would fit the PORT/CAR2 postseismic motions. Since CAR2 has a substantial positive vertical postseismic velocity which is opposite to its coseismic offset (Figure 4), the afterslip near Port Blair must be along the downdip extension of the coseismic rupture. We assume that this applies to the entire length of the rupture and derive an afterslip model, allowing for dislocations on segments 1A, 1B, 1C, 1D, 2A, 3A, and 3B (Figure 1 and Table 1). For simplicity we assume that afterslip on each plane is uniform, that slip is parallel to estimated coseismic slip, and that the slip values are identical on segments 1A, 1B, 1C, and 1D. Inverted afterslip and the corresponding predictions of the afterslip model are shown in Figure 6. We use this model to evaluate the motions expected at the SGPS sites during the period between the earthquake and their respective observation times, then correct the observed SGPS horizontal offsets for these motions. This amounts to a 5 to 10% reduction in westward offset for the Andaman SGPS sites, and a 1 to 10% reduction in westward offsets for Sumatran sites; the reduction is generally about 10% for the large-offset northern Sumatran sites. We find that the resulting effect on coseismic slip models is a negligible reduction in

seismic moment (less than 0.2%), suggesting that the applied correction is reasonable. (The absence of a significant effect on inferred seismic moment is because almost all uncorrected SGPS data is underpredicted by coseismic slip models, and with the above correction model fit improves without a substantial change in inferred coseismic slip simply because the correction reduces the mismatch.) The corrected SOI and Subarya et al. (2006) measurements are given in Tables S3 and S4, respectively.

3 26 December 2004 Coseismic Slip Model

The fault geometry considered by Banerjee et al. (2005) (their Table S2) is guided by aftershock activity and the seismically-determined slab-depth contours (Figure 1) and is in harmony with coseismic uplift and subsidence data from the Andaman Islands and Nicobar Islands. Within the Andaman Islands (north of about 8°) the slab-depth contours are less reliable (e.g., the actual trench axis as mapped by Curray (2005) is offset up to ~ 60 km to the east of the 0-km slab contour of Gudmundsson and Sambridge (1998)). The fault planes used in this study are shown in Figure 1a and described in Table 1. They are based primarily on focal mechanisms of aftershocks (Banerjee et al., 2005), and near-field geodetic data. The locations of these planes are compared with hypocenter locations of earthquakes that occurred from 1915 to 2005, including aftershocks of the December 2004 event (Engdahl et al., 2006), in Figure S4. In general, slab-related seismicity based on teleseismically-determined location algorithms show much scatter and, taken in isolation, allow a modest range of possible slab geometries.

The hypocenter locations in the Engdahl et al. (2006) catalog tend to locate systematically deeper than the chosen fault planes (equivalently, they are systematically offset to the west relative to the chosen fault planes). This is particularly apparent in the cross-section for planes 1D+1H. Rupture planes situated ~ 50 km to the west of the chosen planes 1D+1H, as suggested by the Engdahl et al. (2006) hypocenters, are possible in this area; a model of 30 meters of predominantly dip slip (rake= 105°) on plane 1H (0 to 30 km depth), after shifting it 50 km to the west of its Table 1-location, is found to match simultaneously the 6.0 m horizontal coseismic offset (Figure 5) and the 1.1 m subsidence (Figure 4) at CARN. The precise location of these planes is difficult to judge because fault location trades off with slip in the fitting of the geodetic data. We prefer the chosen locations of planes 1D+1H on the grounds that the slip required to fit the CARN offsets (16.6 meters predominantly dip slip in our preferred model) is more reasonable, but the alternative location cannot be ruled out. Off northern Sumatra near 4°N , well-constrained aftershock locations based on ocean-bottom seismometer (OBS) deployment (Araki et al., 2006) accurately illuminate the slab geometry. Both the OBS-relocated seismicity (Figure 4 of Araki et al. (2006)) and the Engdahl et al. (2006) catalog indicate vigorous aftershock activity down to 50 km depth, supporting the conclusion of Banerjee et al. (2005) that coseismic rupture penetrated relatively deep in this region. The Engdahl et al. (2006)-catalog locations agree well with the OBS-determined aftershock hypocenters in this area, and both coincide well with the segment 3C location (Figure 1), dipping 11° from depth 0 to 30 km, but the OBS seismicity indicates a somewhat shallower dip from 30 to 50 km: about 20°

compared with 35° for our segment 3A. We choose the steeper dip for consistency with Banerjee et al. (2005), who noted the many aftershocks in this area associated with dip $\sim 30^\circ$.

The fit of Model M3 of Banerjee et al. (2005) to the near-field GPS uplifts and horizontal offsets, shown in Figures 4 and 5, respectively, supports the overall prescription of fault geometry. In this study we have further revised the Banerjee et al. (2005) fault geometry by adding an additional possible coseismic rupture plane deep on the Nicobar segment (subsegment 2A in Table 1). Because of the limitations of the dataset used by Banerjee et al. (2005), they assumed uniform slip on all Andaman (segment-1) subsegments and grouped the Nicobar subsegments 2B and 2C together into one plane. Here we allow for independent slip of all tabulated subsegments, with the restriction that variable rake on the Andaman subsegments obeys the relationship given in Table 1, assuming a single relative plate motion direction for the entire segment. We also prescribe fixed $\lambda_1 = 105^\circ$ (Banerjee et al., 2005) and $\lambda_3 = 90^\circ$, which is consistent with the sense of slip illuminated by seismic focal mechanisms (Banerjee et al., 2005).

Near-field coseismic offsets are sensitive to details that are outside the model space being considered, e.g., relatively short-scale slip variations, heterogeneity in elastic structure, etc. Since such factors are not accounted for, it is not possible to fit the near-field observations to within their formal errors. Therefore we increase these errors in order to represent the uncertain amount of signal that lies outside the model space. We assign nominal 20 cm standard errors to east and north components of the near-field coseismic offsets (Figure 5). (Results depend little on the assigned near-field GPS er-

rors within generous limits.) Vertical offsets from 12 sites in the Andaman Islands (11 SOI sites and 1 site from Jade et al. (2005)) and 18 sites in northern Sumatra (Subarya et al., 2006) that are closest to the southern termination of rupture are also used in the inversions for fault slip. Similarly to the Andaman horizontal offset estimates, we assign nominal 20 cm standard errors to all vertical offset estimates.

Slip on a subsegment is related to static surface displacement using the source response functions calculated with the method of Pollitz (1996). This yields theoretical displacements in a layered spherical geometry with a spherical harmonic expansion, and global Earth model PREM with isotropic elastic parameters is used for this purpose. For far-field displacements, we truncate the spherical harmonic expansion at degree $l = 1000$, equivalent to a horizontal wavelength of about 40 km. For near-field displacements, we increase the accuracy of the calculation by means of a commonly-employed expedient. First, the static deformation is calculated exactly on an elastic half-space using the formulae of Okada (1985). Second, the static deformation is calculated on the spherically-layered structure (i.e., PREM) with an expansion up to $l = 1000$; third, it is calculated on a homogeneous sphere with an expansion up to $l = 1000$. The static deformation is a composite of that determined in steps 1 and 2 minus that determined in step 3. This procedure is valid where sphericity effects are negligible (i.e., the near field), and it avoids the need of conducting a spherical harmonic expansion up to very large degree.

There are altogether 316 data constraints on the slip model: 286 constraints resulting from 143 horizontal GPS vectors and 30 constraints re-

sulting from the included vertical offsets. Least squares inversion of the dataset yields estimates of slip values for selected segments. We find that satisfactory fits to all data may be obtained without the deeper Andaman subsegments 1A, 1B, and 1C, and the deeper Nicobar segment 2A. Inversions with any of these segments, or combinations thereof, generally yield negative slip, and therefore zero slip is assigned to these subsegments in all inversions. Inversions in which slip on Sumatran segments 3A and 3C are independent yield ~ 25 m slip on the deeper segment 3A and ~ 3 m slip on the shallower segment 3C, and the tradeoff in slip between the two is not well resolved. To stabilize the inversion we impose the constraint $u_{3A} = u_{3C}$. Results for three different models are given in Table 2. Models A and B each involve the shallow Nicobar segment 2C. In Model A, the slip of the two Nicobar segments 2B and 2C are constrained to be equal ($u_{2B} = u_{2C}$), and in Model B only the shallow Nicobar slip is considered ($u_{2B} = 0$, u_{2C} variable). In Model C only the intermediate Nicobar slip is considered (u_{2B} variable, $u_{2C} = 0$). The two models (A and B) which involve the shallow Nicobar segment 2C have associated reduced χ^2 misfits of 2.32 and 4.40, respectively, and perform worse than Model C, which involves only the intermediate Nicobar segment 2B (Figure 8) with $\chi^2 = 2.07$. The substantially improved fit in Model C is most apparent in the fit to the near-field horizontal and vertical offsets (e.g., Figure 4). Model B, which omits the intermediate segment altogether, fits the dataset much worse despite the very large slip value $u_{2C} = 56$ m.

4 28 March 2005 Coseismic Slip Model

A wealth of horizontal GPS time series is available to constrain the offsets of the 28 March 2005 Nias earthquake, primarily because the source region was near the already-operating SUGAR network maintained by Caltech and the Indonesian Institute of Sciences (LIPI). Several of the time series obtained for analysis of the 26 December 2004 offset continue through the time of the Nias earthquake and constrain the coseismic offsets of the Nias earthquake. These time series are augmented by measurements at other regional sites available only after the 2004 earthquake; GPS sites with time series commencing after December 2004 include BSIM, LEWK, LWHA, and PSMK of the SUGAR network. We have assembled corresponding time series at 49 regional and global sites. Time series from site SUGAR network site PBAI are shown in Figure 9; time series from nine other sites are shown in Figure S6. Early post-Nias deformation is as vigorous as it was immediately after the Sumatra-Andaman earthquake (Figures 9 and S6). Therefore we adopt the same procedure as before for estimating the coseismic offset, i.e., estimation of best-fitting lines through the 18-day pre-seismic and 7-day postseismic portions of the time series, and evaluation of the positions on these lines at times t_0 and t_1 , respectively. Examples of the pre-seismic and post-seismic averages are given in Figures 9 and S6. Choosing $t_1 - t_0 = 1$ day, the resulting coseismic horizontal displacement field is given in Table S5 and plotted in Figure 10.

To obtain a coseismic slip model we are guided by the fault geometry determined by Ji (2005) and the depth contours of the downgoing slab

obtained by Gudmundsson and Sambridge (1998) (Figure 1). The former prescribes a slip surface striking 325° and dipping 15° that optimally fits seismic waveforms. Since most seismic slip is restricted to the depth range 20 - 40 km, we choose approximately these depths for the upper and lower edge depths of all planes. We have slightly adjusted the slip surface defined by Ji (2005) to conform better with the local slab depth contours (Figure 1b), and extended it in the northwest and southeast directions, resulting in five distinct slip planes (Table 3). The upper and lower edge depths of segment 3, in particular, were adjusted on the basis of a trial-and-error search for these depths, resulting in the best fit to the dataset, other factors being equal. The southernmost segment (segment 5) extends slightly beyond the limit of main aftershock activity (Figure 1). The distribution of data and azimuthal coverage are such as to allow inversion for dip slip and strike slip on all segments, with the exception of the northernmost one (segment 1), on which we prescribe $\text{rake} = 90^\circ$. Three of the coseismic displacement vectors – BSIM, LHWA, and PSMK (Figure 10) – have large displacements that are likely sensitive to shorter length-scale details of the actual slip distribution than we attempt to model, and therefore the formal standard errors in the corresponding displacements are scaled up by 1 to 2 orders of magnitude. The standard deviations of north and east components of all 46 other sites are assigned their formally-determined values from Table S4 (generally a few mm).

Least squares inversion of this dataset for the fault slip parameters yields the slip values and associated uncertainties given in Table 3 and plotted in Figure 11. The slip is concentrated on the relatively deep segment 2 and

relatively shallow segment 3, which accommodate about 12 m and 8 m dip slip, respectively. These slip values and the relatively shallow depth of the segment-3 slip are consistent with the slips and locations of the two most prominent slip maxima in the seismic slip inversion of Ji (2005). Briggs et al. (2006) used a combination of coral microatoll measurements and GPS displacement vectors to obtain a high-resolution slip distribution. The locations and amplitudes of their slip maxima are similar to those of Ji (2005) and agree with the locus of maximum slip between $\sim 1^\circ\text{N}$ and 2.5°N obtained in our study. The concentration of seismic moment release between depths of 14 and 35 km, well to the east of the trench axis, obtained by Briggs et al. (2006) agree well with our inferred slip distribution. Our geodetically-determined model, obtained with a dip of 15° , corresponds to magnitude $M_w = 8.66$. (We use the formula $M_w = (2/3) \log_{10} M_0[\text{dyne} - \text{cm}] - 10.7$ (Hanks and Kanamori, 1979).) This is larger than the magnitude $M_w = 8.5$ obtained by Ji (2005) from seismic wave analysis using the same dip. This suggests a substantial difference between the moment at seismic periods and that determined geodetically, which may imply an additional contribution from afterslip occurring within a short time after the earthquake.

Reduced χ^2 associated with the slip model is 2.16. The overall fit to the dataset is better than suggested by this value since a large fraction of the misfit arises from the misfits at just three sites – SAMP, MSAI and BSIM. For example, omission of MSAI results in a reduced χ^2 of 1.92 with nearly the same slip distribution. Improved fit of these sites may require a combination of more detailed slip on the considered planes plus possibly additional slip extending even further to the southeast. This may apply particularly to

MSAI, which may record slip on an isolated patch near -2°N , 99°E , the site of a cluster of aftershock activity (Figure 1) which is well removed from the main locus of slip.

5 Discussion of the 26 December 2004 Coseismic Slip Model

The best-fitting model is Model C (hereinafter the "preferred model"), which prescribes $\sim 19\text{m}$ slip beneath the Nicobar segment from 15 to 30 km depth (Figure 8) without any shallower or deeper slip along that segment. In addition to fitting near-field horizontal and vertical offsets better than other models, its performance also arises from fitting distant sites PHKT and ARAU better than the other models. Models A and B yield predicted displacements at PHKT that are slightly too small and displacements at ARAU that are slightly too large. The preferred model allows these offsets to be better fit by shifting the locus of displacement towards PHKT with sub-segment 2B. A variation of the preferred model which solves additionally for shallow Nicobar segment slip (u_{2C}) yields almost identical slip and rake values for the other segments but a negative slip of $u_{2C} = \sim -19.5 \pm 3.2 \text{ m}$ on the shallow Nicobar segment, verifying that relatively low or no slip on the shallow Nicobar segment is preferred.

Deep coseismic slip beneath the Sumatra segment (segment 3) was established by Banerjee et al. (2005), and together with the deep slip beneath the Nicobar (2A) and southern Andaman (1D) subsegments, this suggests that slip extending well below 30 km depth characterized the overall rup-

ture from its initiation at 3°N northward to about 9.5°N . Thereafter, the slip of the remaining ~ 600 km of the Andaman segment must be relatively shallow ($\lesssim 30$ km depth) in order to satisfactorily match the vertical GPS data. This follows from comparison of the Banerjee et al. (2005) Model M1 and all other models in Figure 4. Model M1, which includes deep slip along the entire Andaman segment, poorly fits the observed subsidence at Port Blair and several other northern Islands sites.

The pattern of uplift predicted by the preferred model matches observed GPS uplifts on the Nicobar and Andaman Islands (Figure 4) and around northern Sumatra (Figure 12), and it may be compared with the uplift pattern determined by the response of corals to the change in local tide induced by the seafloor uplift/subsidence (Meltzner et al., 2006). The comparison in Figure 13 includes those measurements from Table 1 of Meltzner et al. (2006) indicating at least 5 cm uplift or 5 cm subsidence; absolute vertical movements are generally not possible using satellite imagery of coral reefs. However, field investigations of reefs around Simeulue Island provide a detailed and quantitative description of the uplift patterns near the southern edge of the rupture (Meltzner et al., 2006; their Table 2). The sign of observed movements is generally well predicted except near Simeulue Island (around 2.5°N , 96.0°E), where a small amount of subsidence ~ 20 cm is predicted where small uplift $\gtrsim 20$ cm is measured. Small subsidence of ~ 6 cm is predicted just slightly further east, comparable with observed subsidence of ~ 50 cm at 2.392°N , 96.332°E according to Table 3 of Meltzner et al. (2006). These results suggest that some minor slip may have continued further south to beneath Simeulue Island. Slip heterogeneity around the

southernmost part of the rupture is also suggested by the three-dimensional coseismic offset at R171. The horizontal offset is shown in Figure 3 and the vertical offset in Figure 12, where they are compared with the Model-C prediction. The $\sim 5.7\text{m}$ horizontal offset is satisfactorily matched by the model, but the $\sim 2.1\text{m}$ uplift is underpredicted. The ratio between the vertical and horizontal offsets at R171 is much larger than expected for a site in the hanging wall of an 11° -dipping fault. Subarya et al. (2006) fit the three-dimensional displacement vector at R171 with a very localized slip patch which accomplishes the task of matching the large vertical-to-horizontal offset ratio.

The slip distribution on the preferred model (Figure 8) is consistent with the results of seismic slip inversions (e.g. Ammon et al., 2005) and joint seismic-geodetic inversion (Chlieh et al., 2006). These studies employed a spherical layered Earth 3D model (Ammon et al., 2005) and a layered half-space (Chlieh et al., 2006), and among existing studies they are the most comparable with our results based on a spherical layered 1D Earth model. Referring to Model III of Ammon et al. (2005) (their Figure 5c) and Model G-M9.15 of Chlieh et al. (2006) (their Figure 9), these studies have fault geometry similar to that used in the present study, and slip locations and maxima in good agreement with that determined here. This includes the very deep dip slip of $\sim 20\text{m}$ near 4°N , relatively deep dip slip on the Nicobar segment from 5°N to 8°N , and a moderate amount of oblique slip (3m to $\sim 8\text{m}$) along the Andaman Islands north of $\sim 9^\circ\text{N}$. The slip amplitudes of Chlieh et al. (2006) in the Andaman Islands particular match our slip amplitudes because of their use of geodetic data from this region. The

persistence of high-amplitude slip (15 to 20 m) from 3°N to $\sim 9^\circ\text{N}$ is also a common feature of the Model G-M9.15 of Chlieh et al. (2006) and the present study; estimated slip amplitudes along the Nicobar segment are about 50% smaller in Model III of Ammon et al. (2005). This suggests that despite the vigorous aftershock activity around the shallow Nicobar segment – segment 2C (Figure 1a) – the associated coseismic slip was relatively low.

The seismic moment of the preferred model is $M_0 = 7.62 \times 10^{22}$ Nm, corresponding to $M_w = 9.22$. (Again, we use the formula $M_w = (2/3) \log_{10} M_0$ [dyne – cm] – 10.7, the definition given by Hanks and Kanamori (1979).) Model III of Ammon et al. (2005) has a seismic moment of 6.5×10^{22} Nm, corresponding to $M_w = 9.17$. The apparent excess geodetic moment over the seismic moment is 17%. Ammon et al. (2005) find that at seismic frequencies up to 2000 sec, relatively little slip occurred on the Andaman segment. Their model, which has most seismic slip finished in about 10 minutes after the mainshock, is further consistent with the free oscillation spectra at periods up to one hour (Park et al., 2005). Park et al. (2005) note that slow slip confined to the period after seismic slip terminated but up to only one hour after the mainshock would inefficiently excite the observed free oscillations because of phase cancellation. Slow slip distributed over a period of hours after seismic slip terminated, however, would have little effect on the free oscillation amplitudes, which would then be shaped primarily by the seismic slip accumulated during the first 10 minutes. Therefore, it is tempting to suggest that the several meters of slip on the Andaman segment, needed most notably to explain the several meters horizontal offsets at Islands sites (Figure 5) and the apparent geodetic-seismic moment discrepancy, must

have occurred at periods far greater than one hour. However, this interpretation is not supported by analysis of CGPS time series. Vigny et al. (2005) showed that little motion occurred at Phuket (PHKT) after about 10 minutes. Moreover, their various PHKT-offset estimates differ from our own estimate by only 4%. If the geodetic-seismic moment discrepancy were real, then one would expect a much larger difference. Hashimoto et al. (2006b) has further shown that CGPS sites in northern Thailand, which are particularly sensitive to motions along the Andaman Islands, exhibit little resolvable motions after the first 10 to 20 minutes. Analysis of joint seismic and geodetic datasets (Chlieh et al., 2006) yields a coseismic slip model with slippage occurring during the first ~ 10 minutes and with predictions that are in harmony with both datasets. The range of seismic moment in the acceptable models of Chlieh et al. (2006) is 6.7 to 7.0×10^{22} Nm, only 8 to 12% lower than the geodetic moment inferred in this study. (The seismic moment of their Model G-M9.15 is 6.93×10^{22} Nm, 9% lower than inferred in the present study.) Until direct evidence from hourly or epoch GPS solutions becomes available, we surmise that the apparent geodetic-seismic moment discrepancy is artificial or explicable with small amounts of aseismic slip beyond the first hour after the mainshock.

The remaining seismic-moment discrepancy may reflect simply the uncertainties inherent in each approach. The imaging power of each study is good based on formal resolution tests (e.g., Figures 4a and 4b of Chlieh et al. (2006)) and the relatively small (~ 1 to 2 meters) formal standard deviations of our slip estimates (Table 2). However, both the regularization used in distributed-slip inversions (Ammon et al., 2005; Chlieh et al., 2006)

and the assumption of uniform slip on pre-specified dislocation planes (this study) will inevitably result in inaccurate slip distributions, with a corresponding uncertainty of the net seismic moment estimated in each study. If far-field GPS measurements are a reliable guide to the earthquake size, we suggest that either Model G-M9.15 of Chlieh et al. (2006) or the preferred model of the present study, each of which fit the far-field GPS data with a layered structure, provide a useful estimate of the net seismic moment.

6 Secondary Source in the Aceh Basin?

On the basis of tsunami amplitudes and arrival times in NW Sumatra during the 2004 Sumatra-Andaman earthquake, Plafker et al. (2006) propose a secondary source in the Aceh basin. In order to produce the very large (up to 39m) runups along the coast of NW Sumatra, they envision coseismic slip on a steeply-dipping splay structure accommodating $\gtrsim 15\text{m}$ dip slip. The proposed structure would be on the western edge of the Aceh basin, along the eastern edge of a sharp shelf break, a location which is coincident with the West Andaman Fault (Sieh and Natawidjaja, 2000). A set of aftershocks within the overriding plate is localized in this area (area C in Figure 3 of Araki et al. (2006)), suggestive of some coseismic slip on a structure in this area. The geodetic data considered here hint at the existence of this structure through its kinematic implications. Dip slip on splay faults during the 1964 Alaska earthquake served to produce a kinematic discontinuity between the deeper megathrust and shallower megathrust such that a substantial amount of deeper slip was transferred to the splay faults, resulting

in relatively little slip of the shallower megathrust (Plafker, 1969). A hypothetical splay fault located near the boundary of Sumatran segments 3A and 3C could play the same role. We summarize the results of geodetic inversions involving variations of Model C in Figure 14; the result of Model C itself is depicted in Figure 14c. One variation allows the dip slip of segments 3A and 3C to be independent. Resulting slip values on other segments are nearly identical to Model-C slip values, but the estimated segment-3A and 3C slip values are $25.6 \pm 1.7\text{m}$ and $2.7 \pm 2.1\text{m}$, respectively, with associated χ^2 of 1.93 (Figure 14b). We further consider a hypothetical high-angle thrust ("splay fault" in Figure 14a), approximately coincident with the West Andaman Fault, placed with a lower edge at the upper edge of segment 3A. Fits to the geodetic data are practically insensitive to possible slip along this segment, which would involve primarily vertical motions on a fault that is distant from most of the GPS sites. When dip slip of 20m is assigned to this segment (Figure 14a) and remaining slip parameters are inverted as before, the result is $u_{3A} = 20.1\text{m}$ and $u_{3C} = 2.9\text{m}$, with $\chi^2 = 1.96$. The robust feature of these test results is the disparity in slip between segments 3A and 3C, regardless of the possible value of slip on the splay fault. The discontinuity in dip slip between segments 3A and 3C need not be as large as this, since Model C yields a reasonable fit to the dataset with equal amounts of slip on both segments. However, these inversion results – which both have a significantly better fit than Model C – suggest some measure of kinematic discontinuity between the deeper and shallower slip on the megathrust in this area. If real, then the disproportionate amount of aftershock activity deeper than 30 km imaged by Araki et al. (2006) would reflect the much greater coseismic slip

having occurred along the deeper section of the megathrust.

7 Conclusions

We have assembled new datasets of GPS offsets for the 26 December 2004 Sumatra-Andaman and 28 March 2005 Nias earthquakes. Our compilation includes new data for 64 sites for the Sumatra-Andaman earthquake, 53 of which are continuous GPS providing far-field measurements and 11 of which are campaign GPS providing near-field measurements. These data are augmented by:

- (1) An additional non-redundant coseismic vector offset in the Andaman Islands, one of several such vector offsets given by Jade et al. (2005),
- (2) static offsets estimated at 55 non-redundant far-field sites by Vigny et al. (2005) (48 of which are continuous GPS measurements and the other 7 campaign GPS measurements in Thailand), and
- (3) 23 northern Sumatra sites by Subarya et al. (2006) (all of which are campaign GPS measurements). The 12 near-field campaign measurements and 18 of the 23 northern Sumatra campaign measurements contribute useful vertical displacements. The composite dataset has altogether 143 horizontal displacement vectors and 30 vertical displacement vectors.

All CGPS offsets are here derived by projecting the pre-earthquake displacements to the time just before the mainshock, and the post-earthquake displacements to a time point one day after the mainshock. For the Sumatra-Andaman earthquake, the campaign data involve post-earthquake motions occurring anywhere from 10 days to 7 weeks after the mainshock. Post-

earthquake movements during the first three weeks at Port Blair are a small fraction (about 8%) of the coseismic offset. We perform a small correction of Andaman and northern Sumatra SGPS data by deriving an afterslip model based on available CGPS time series, then evaluating the effect of this afterslip in appropriate time intervals at the SGPS sites. In this manner the SGPS data are corrected for postseismic offsets.

Our compilation also includes horizontal displacement data for 49 sites for the Nias earthquake, all of which are continuous GPS sites. The distribution of sites with respect to the Sumatra-Andaman rupture has a preponderance of sites at distances $\gtrsim 500$ km from the rupture, a dearth of sites within the distance range 50 to 500 km, and a good number of sites within 50 km of the rupture in the Andaman Islands. The distribution of sites with respect to the Nias earthquake is much more uniform in terms of distance from the rupture. In both cases, the site distributions afford a fairly detailed picture of the slip distribution of each earthquake, including the centers of dominant slip and their approximate extent in depth, in approximate agreement with the results of more detailed seismic slip inversions.

Acknowledgments. We greatly appreciate data made available by BAKO-SURTANAL (SAMP), IGS (BAKO, NTUS), the Department of Survey and Mapping Malaysia (MASS sites), Prof. Narong Hemmakorn at the King Monkut’s Institute of Technology Ladkrabang, Thailand (CPN, KMI), Prof. Tharadol Komolmis, Chiang Mai University, Thailand (CHMI), Dr. Susumu Saito (NICT sites), and the Tectonics Observatory at Caltech, the Indonesian Institute of Sciences (LIPI) and Scripps Orbit and Permanent Array Center (SuGAR network). We also thank Prof. M. Hashizume for his efforts

of establishing GPS monitoring stations in Thailand. John Paul (CERI Memphis) established the CGPS station CAR2.

References

- Ammon, C., Ji, C., Thio, H.-K., Robinson, D., Ni, S., Hjorleifsdottir, V., Kanamori, H., Lay, T., Das, S., Helmberger, D., Ichinose, G., Polet, J., and Wald, D. (2005). Rupture process of the 2004 Sumatra-Andaman earthquake. *Science*, 308:1133–1139.
- Araki, E., Shinohara, M., Obana, K., Yamada, T., Kaneda, Y., Kanazawa, T., and Suyehiro, K. (2006). Aftershock distribution of the 26 december 2004 sumatra-andaman earthquake from ocean bottom seismographic observation. *Earth Planets Space*, 58:113–119.
- Banerjee, P., Pollitz, F., and Bürgmann, R. (2005). Size and duration of the great 2004 Sumatra-Andaman earthquake from far-field static offsets. *Science*, 308:1769–1772.
- Bilham, R., Engdahl, E., Feldl, N., and Satyabala, S. (2005). Partial and complete rupture of the Indo-Andaman plate boundary 1847-2004. *Seismol. Res. Lett.*, 76:299–311.
- Briggs, R., Sieh, K., Meltzner, A., Natawidjaja, D., Galetzka, J., Suwargadi, B., Hsu, Y.-J., Simons, M., Hananto, N., Suprihanto, I., Prayudi, D., Avouac, J.-P., Prawirodirdjo, L., and Bock, Y. (2006). Deformation and slip along the Sunda megathrust in the Great 2005 Nias-Simeulue earthquake. *Science*, 311:1897–1901.

- Chlieh, M., Avouac, J.-P., Hjorleifsdottir, V., Song, T.-R., Ji, C., Sieh, K., Sladen, A., Hebert, H., Prawirodirdjo, L., Bock, Y., and Galetzka, J. (2006). Coseismic slip and afterslip of the Great (mw 9.15) Sumatra-Andaman earthquake of 2004. *Bull. Seismol. Soc. Am.*, submitted.
- Curray, J. (2005). Tectonics and history of the Andaman Sea region. *J. Asian Earth Sciences*, 25:187–232.
- Engdahl, E., Villasenor, A., DeShon, H., and Thurber, C. (2006). Teleseismic relocation and assessment of seismicity (1918-2005) in the region of the 2004 Mw 9.0 Sumatra-Andaman and 2005 Mw 8.6 Nias Island great earthquakes. *Bull. Seismol. Soc. Am.*, submitted.
- Gahalaut, V., Nagarajan, B., Catherine, J., and Kumar, S. (2006). Constraints on 2004 Sumatra-Andaman earthquake rupture from GPS measurements in Andaman-Nicobar Islands. *Earth Planet. Sci. Lett.*, in press.
- Gudmundsson, O. and Sambridge, M. (1998). A regionalized upper mantle (RUM) model. *J. Geophys. Res.*, 103:7121–7136.
- Hanks, T. and Kanamori, H. (1979). A moment magnitude scale. *J. Geophys. Res.*, 84:2348–2350.
- Hashimoto, M., Chhoosakul, N., Hashizume, M., Takemoto, S., Takiguchi, H., Fukada, Y., and Fujimori, K. (2006a). Crustal deformations associated with the Great Sumatra-Andaman earthquake deduced from continuous GPS observation. *Earth, Planets, Space*, 58:127–139.
- Hashimoto, M., Hashizume, M., Takemoto, S., Fukada, Y., Fujimori, K.,

- Takiguchi, H., Takiguchi, H., Satomura, M., Otsuka, Y., and Saito, S. (2006b). Postseismic deformations following the Sumatra-Andaman and nias earthquakes detected by continuous GPS observation in SE Asia. *Seismol. Res. Lett.*, 77:289.
- Herring, T. (2005). GLOBK: Global Kalman Filter VLBI and GPS Analysis Program, v.10.2. *Mass. Inst. of Tech., Scripps Inst. Oceanogr.*
- Jade, S., Ananda, M., Kumar, P., and Banerjee, S. (2005). Co-seismic and post-seismic displacements in andaman and nicobar islands from GPS measurements. *Current Science*, 88:1980–1984.
- Ji, C. (2005). Updated result of the 05/03/28 (Mw 8.5), Sumatra earthquake. <http://www.gps.caltech.edu/~jichen/Earthquake/2005/sumatra/sumatra.html>.
- King, R. and Bock, Y. (2005). Documentation for the GAMIT GPS Analysis software, release 10.2. *Mass. Inst. of Tech., Scripps Inst. Oceanogr.*
- Lay, T., Kanamori, H., Ammon, C., Nettles, M., Ward, S., Aster, R., Beck, S., Bilek, S., Brudzinski, M., Butler, R., DeShon, H., Ekström, G., Satake, K., and Sipkin, S. (2005). The Great Sumatra-Andaman earthquake of 26 December 2004. *Science*, 308:1127–1132.
- Meltzner, A., Sieh, K., Abrams, M., Agnew, D., Hudnut, K., Avouac, J.-P., and Natawidjaja, D. (2006). Uplift and subsidence associated with the Great Aceh-Andaman earthquake of 2004. *J. Geophys. Res.*, 111:doi:10.1029/2005JB003891.

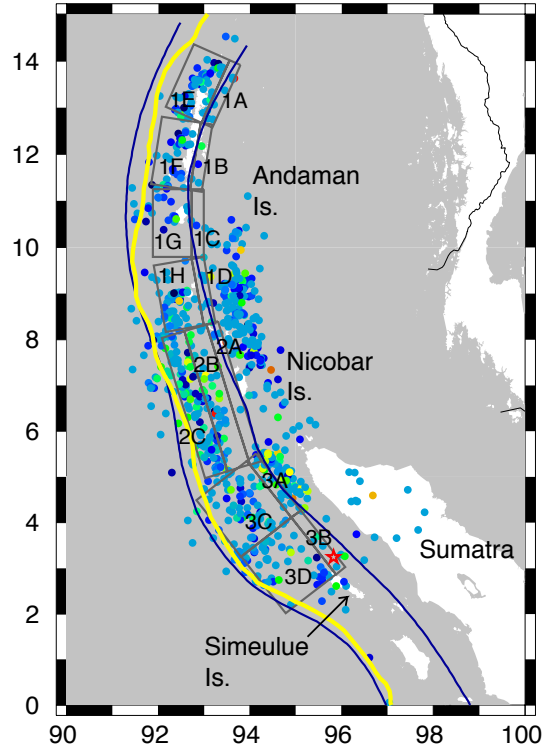
- Okada, Y. (1985). Surface deformation due to shear and tensile faults in a half-space. *Bull. Seismol. Soc. Am.*, 75:1135–1154.
- Park, J., Song, T.-H., Tromp, J., Okal, E., Stein, S., Roullet, G., Clevede, E., Laske, G., Kanamori, H., Davis, P., Berger, J., Braitenberg, C., Van Camp, M., Lei, X., Sun, H., Xu, H., and Rosat, S. (2005). Earths free oscillations excited by the 26 December 2004 Sumatra-Andaman earthquake. *Science*, 308:1139–1144.
- Paul, J., Smalley, R., Bilham, R., Lowry, A., and Batacharjee, A. (2005). Postseismic deformation in the central Andaman Islands. *EOS. Trans. AGU*, 86:Abstract U11B–0838.
- Plafker, G. (1969). Tectonics of the march 27, 1964 alaska earthquake. *U.S. Geological Survey Professional Paper*, 543-I:74p.
- Plafker, G., Nishenko, S., Cluff, L., and Syahril, M. (2006). The cataclysmic 2004 tsunami on NW Sumatra – Preliminary evidence for a near-field secondary source along the western Aceh Basin. *Seismol. Res. Lett.*, 77:231.
- Pollitz, F. F. (1996). Coseismic deformation from earthquake faulting on a layered spherical earth. *Geophys. J. Int.*, 125:1–14.
- Pollitz, F. F., Banerjee, P., and Bürgmann, R. (2005). Postseismic relaxation following the great 2004 Sumatra-Andaman earthquake on a compressible self-gravitating Earth. *Geophys. J. Int.*, in press.
- Sieh, K. and Natawidjaja, D. (2000). Neotectonics of the Sumatran fault, Indonesia. *J. Geophys. Res.*, 105:28295–28326.

- Stein, S. and Okal, E. (2005). Speed and size of the Sumatra earthquake. *Nature*, 434:581–582.
- Subarya, C., Chlieh, M., Prawirodirdjo, L., Avouac, J.-P., Bock, Y., Sieh, K., Meltzner, A., Natawidjaja, D., and McCaffrey, R. (2006). Plate-boundary deformation of the great Aceh-Andaman earthquake. *Nature*, 440:doi:10.1038/nature04522.
- Vigny, C., Simons, W., Abu, S., Bamphenyu, R., Satirapod, C., Choosakul, N., Subarya, C., Socquet, A., Omar, K., Abidin, H., and Ambrosius, B. (2005). GPS in SE Asia provides unforeseen insights on the 2004 megathrust earthquake. *Nature*, 436:201–206.

(A) Sumatra-Andaman earthquake

M>4 Aftershocks

26 Dec 2004 -5 Jan 2005



(B) Nias earthquake

M>4 Aftershocks

28 Mar - 10 Apr 2005

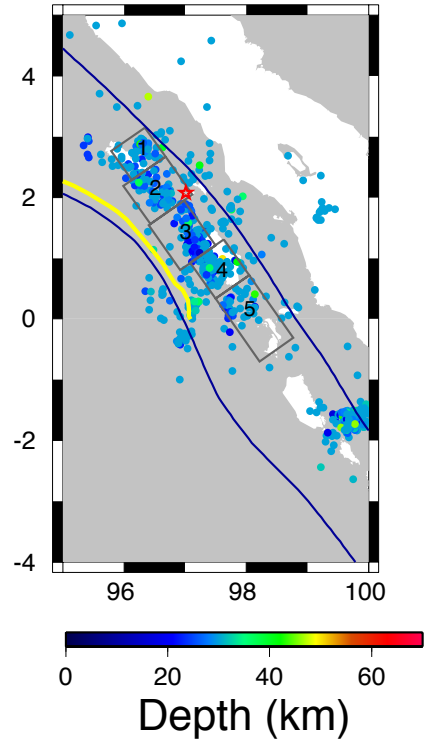


Figure 1: Aftershock activity following the (a) 2004 Sumatra-Andaman and (b) 2005 Nias earthquakes, from the NEIC catalog. Superimposed are the fault planes used in dislocation modeling of the two earthquakes, from Tables S1 and S4, identified by the numerals. Fault labels 1, 2, and 3 identify subsegments that are loosely referred to as Andaman, Nicobar, and Sumatran segments, respectively. Dark blue curves are the 0 and 50 km slab depth contours of Gudmundsson and Sambridge (1998). Yellow curve is the trench axis determined by Curray (2005).

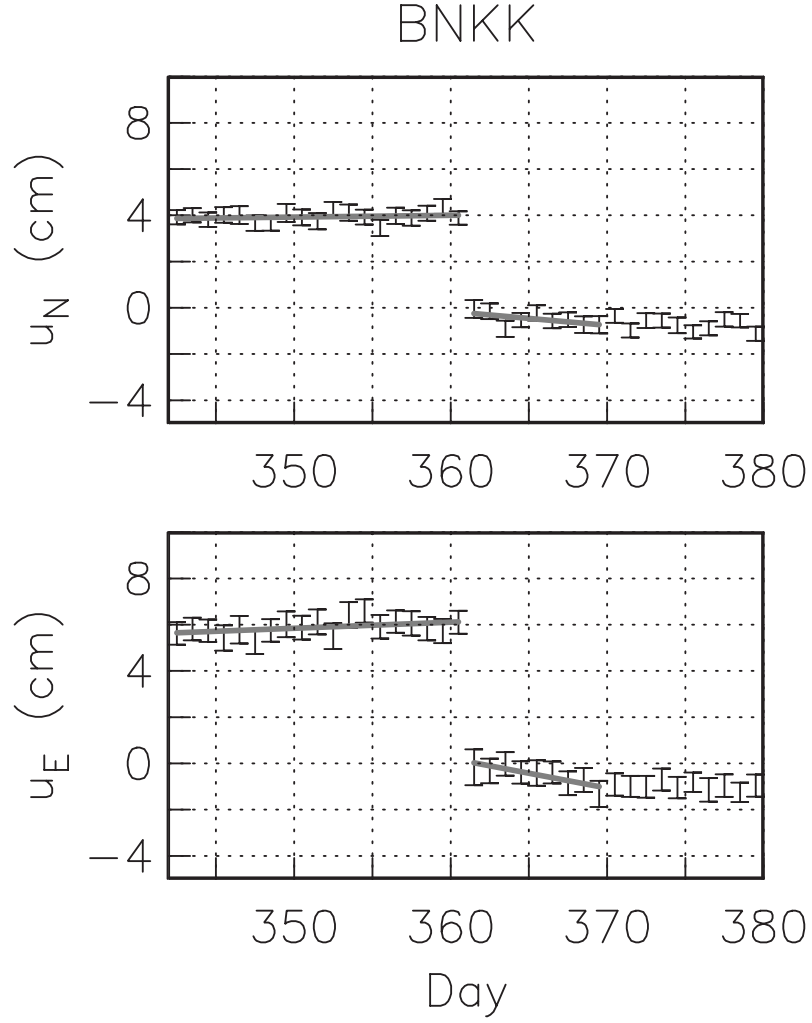


Figure 2: Observed GPS time series following the 26 December 2004 earthquake with $1\text{-}\sigma$ errors at continuous GPS site PHKT (site location in Figure 3). u_E and u_N refer to east- and northward displacement, respectively. Day numbers refer to the year 2004. Superimposed in thick gray are the straight-line fits to 18-day portions of the pre-seismic and 9-day portions of the post-seismic time series.

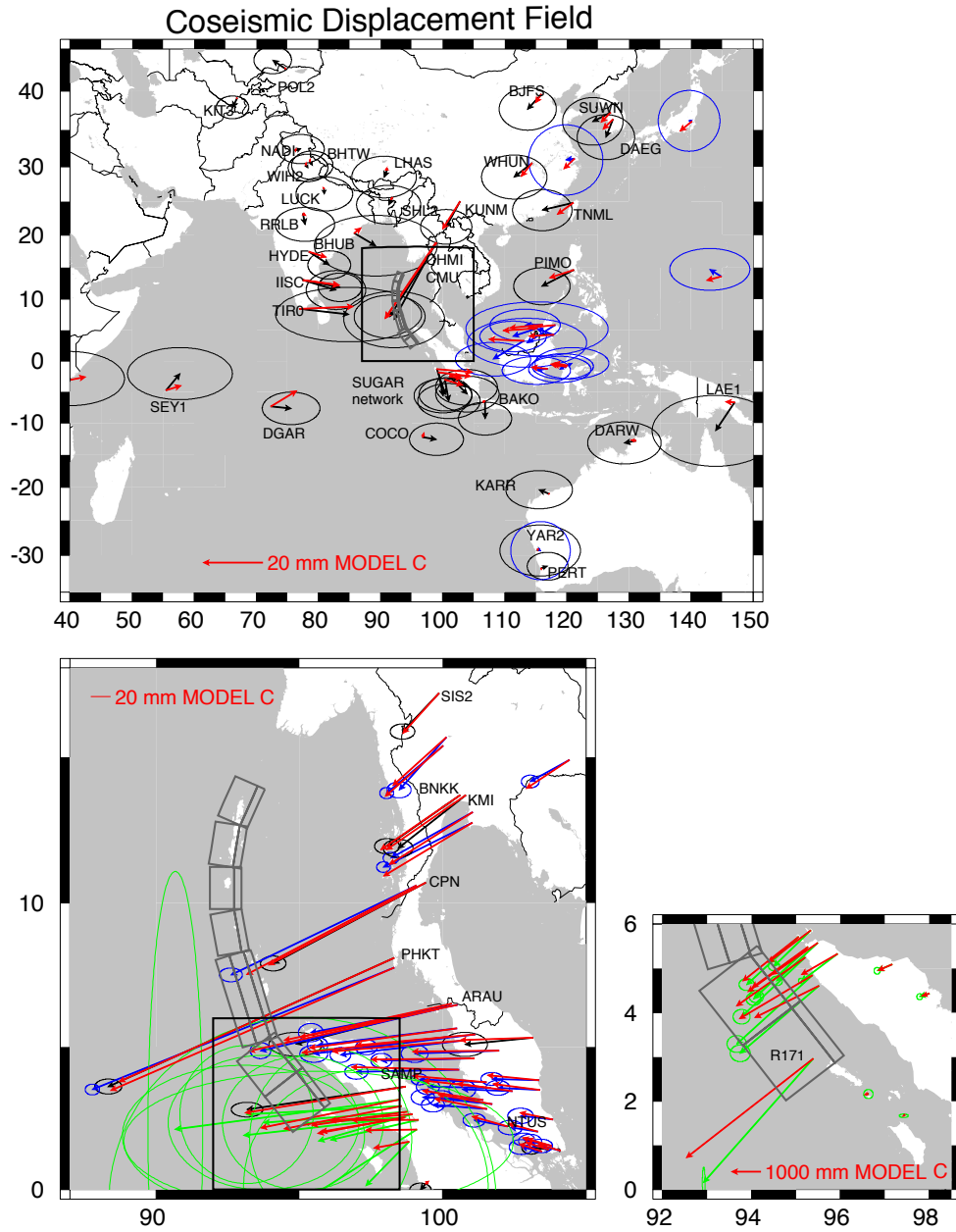


Figure 3: Coseismic horizontal displacement field of the 26 December 2004 earthquake determined in this study, shown by black vectors with 95% error ellipses, together with the "corrected" coseismic offsets derived from Tables 1 and 2 of Vigny et al. (2005) (see text), shown by the blue vectors, and coseismic offsets derived from campaign GPS from Table S1 of (Subarya et al., 2006), shown by the green vectors. The corresponding prediction of slip-Model C (Table 2), the preferred model, is shown by the red vectors. Site labels are given for those CGPS sites which are re-processed in this study. Gray lines indicate the fault planes used to obtain Model C.

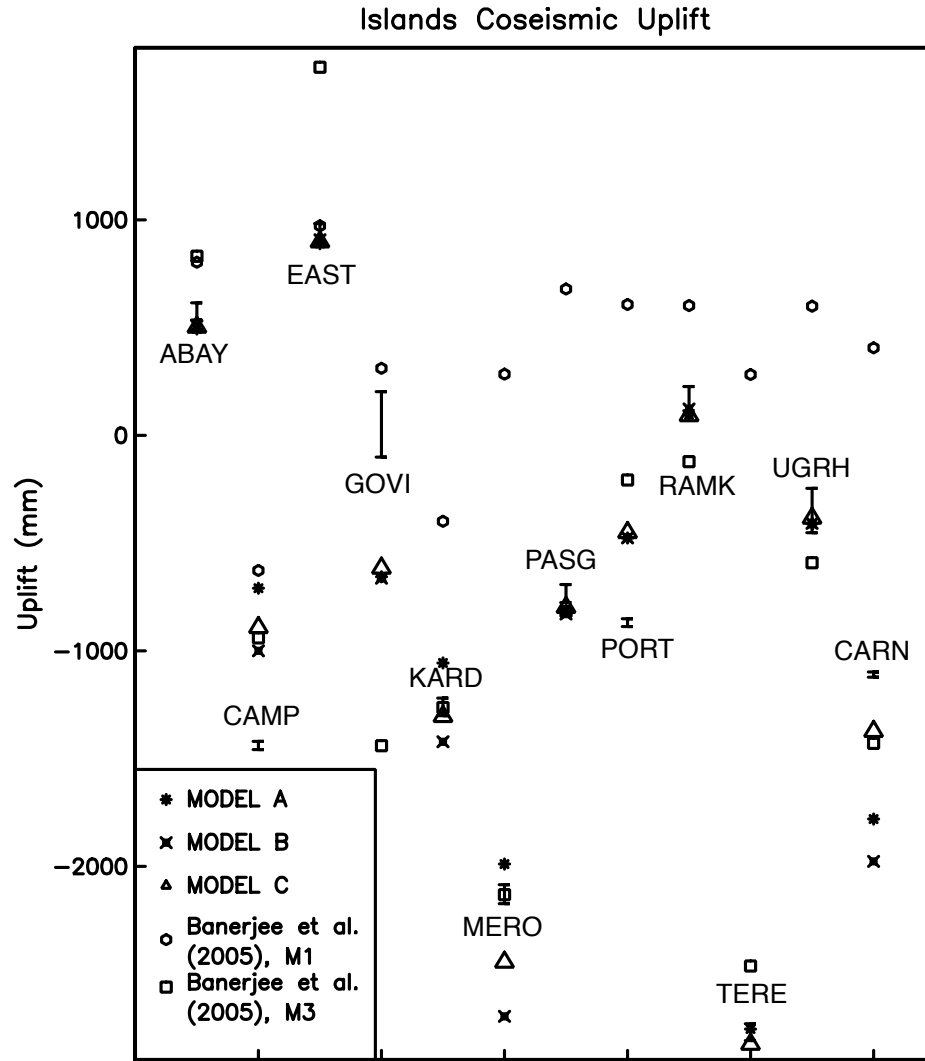


Figure 4: Vertical campaign-GPS displacements along the Andaman and Nicobar Islands determined at 11 SOI sites and at Car Nicobar (Jade et al., 2005) together with various model predictions. Labels refer to site locations given in Figure 5

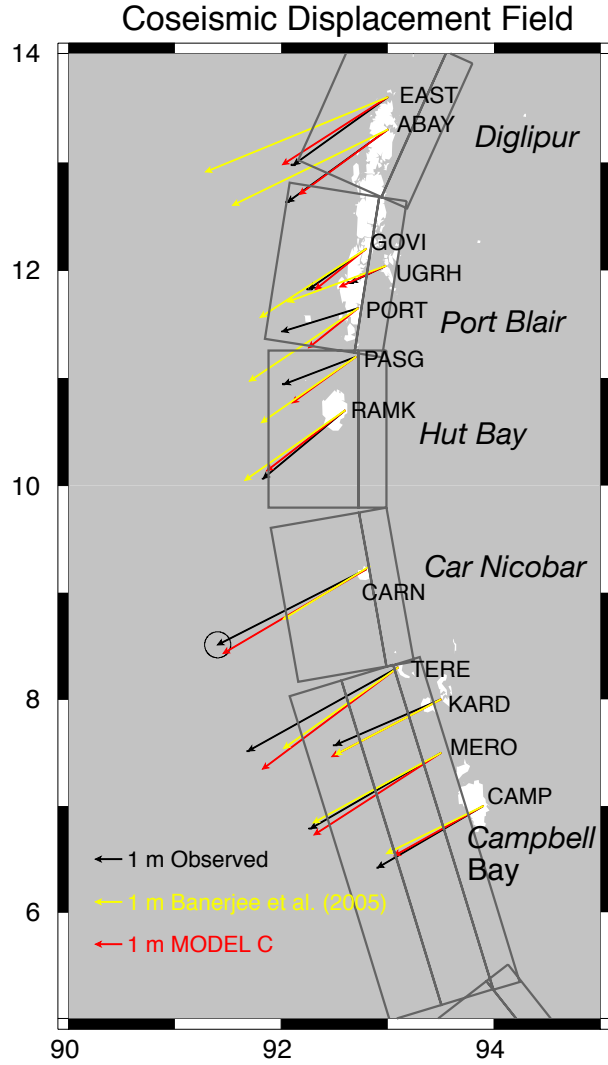


Figure 5: Horizontal near-field campaign-GPS displacements along the Andaman and Nicobar Islands determined at 11 SOI sites and at Car Nicobar (Jade et al., 2005) together with the predictions of Model M3 Banerjee et al. (2005) and Model C.

1 - 50 Days Postseismic Displacement

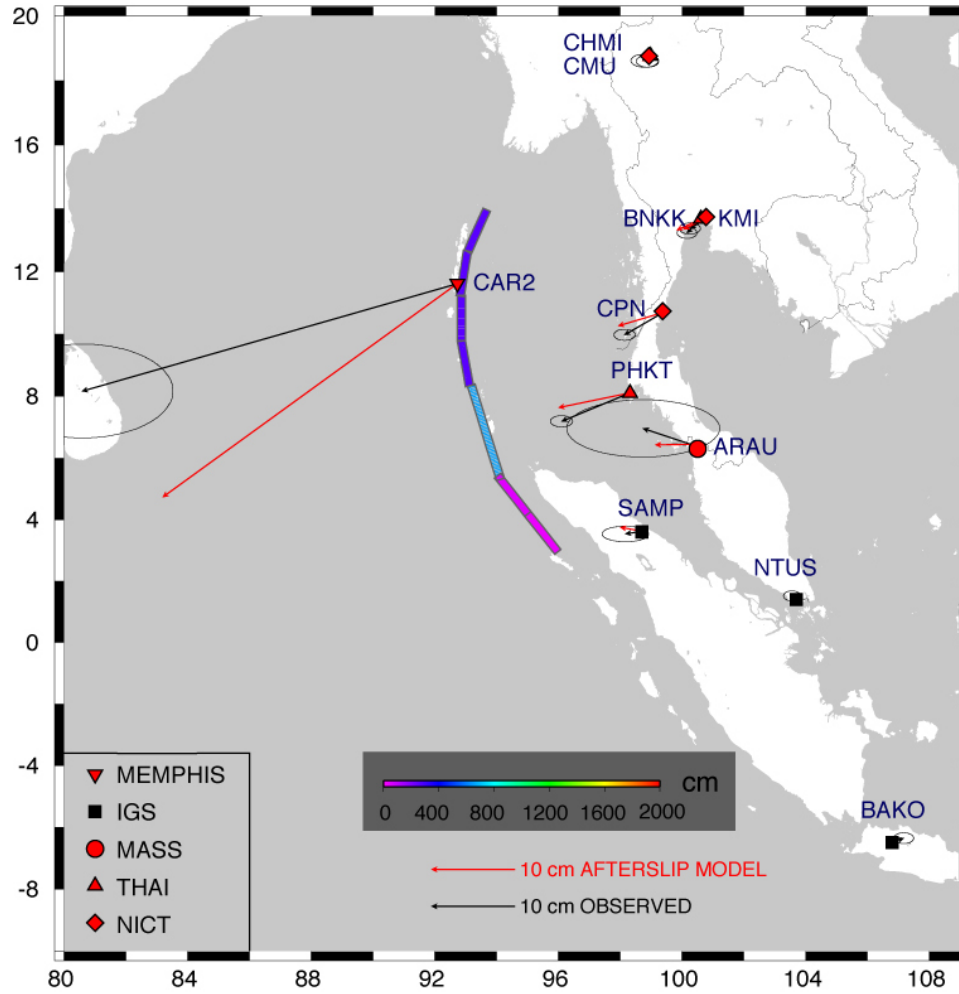


Figure 6: Horizontal displacements of various CGPS sites during the first 50 postseismic days following the Sumatra-Andaman earthquake. The estimate at CAR2 in the Andaman Islands is a logarithmic extrapolation based on data collected from days 10 to 100 after the earthquake (Figure 7). The corresponding predictions of an afterslip model are shown with the red vectors. The slip estimated on the afterslip planes are 2.9 m (planes 1A, 1B, 1C, 1D), 6.0m (plane 2A), 0.8m (plane 3A), and 0.4m (plane 3B).

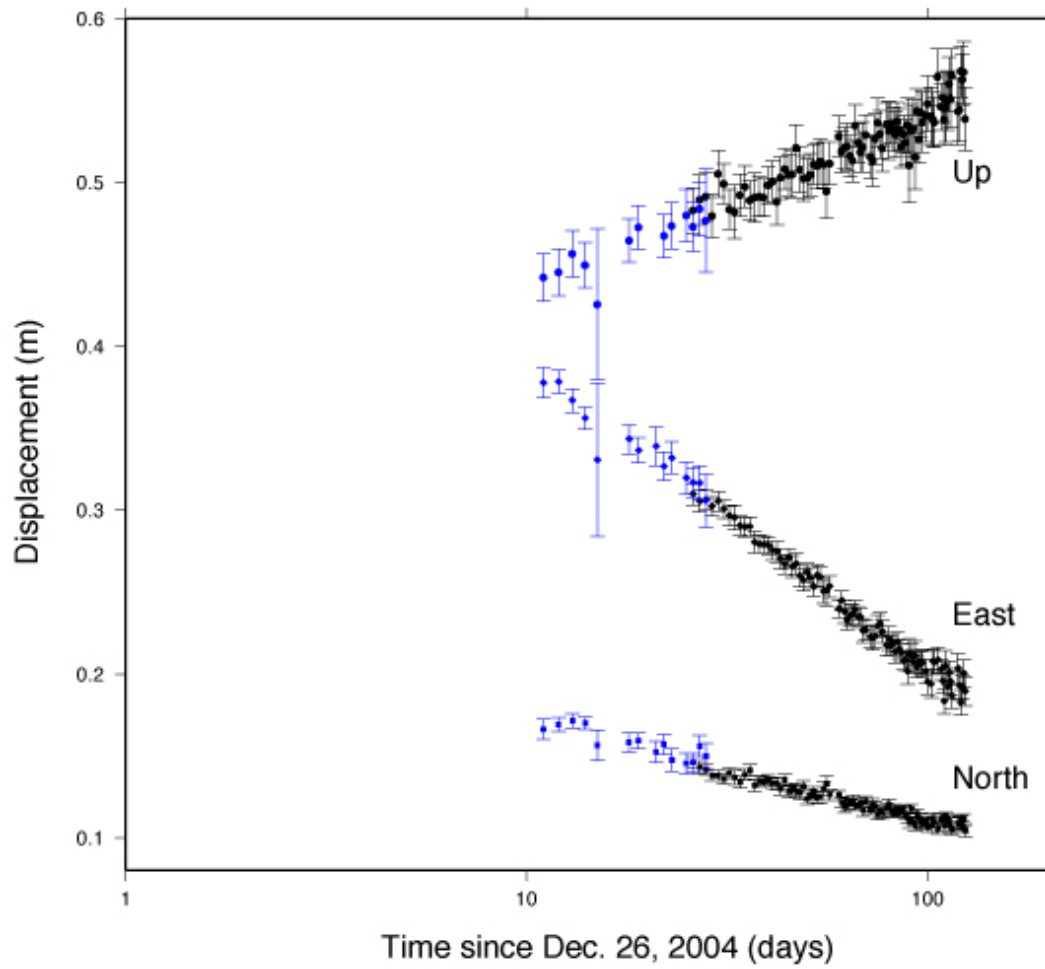


Figure 7: Composite of three-component time series collected at CGPS sites PORT and CAR2, both located at Port Blair, on a log-linear plot. Note the linear trend of each time series, conforming to a $\log(t)$ function dependence for each composite time series.

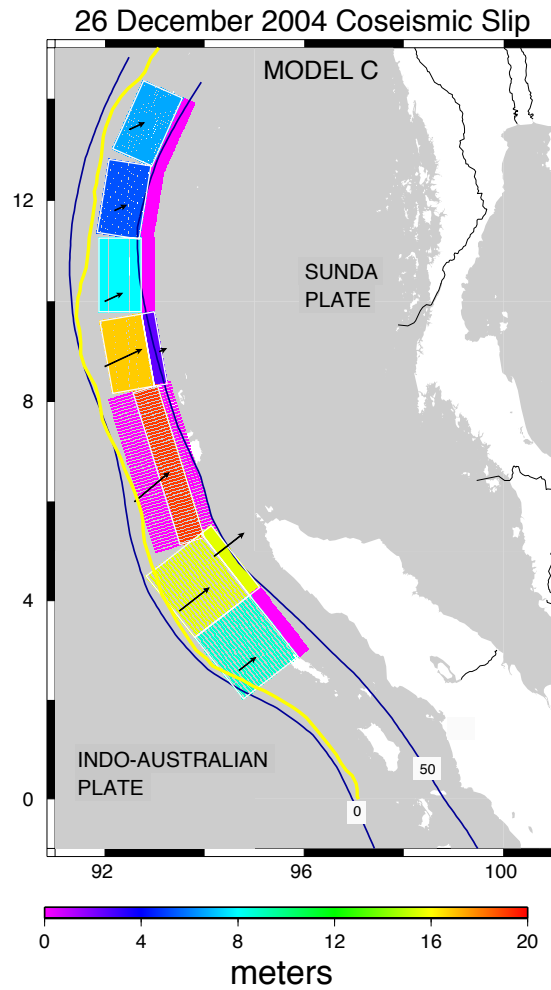


Figure 8: Coseismic slip of the Sumatra-Andaman earthquake from inversion of the integrated continuous and campaign GPS dataset using Model C. Arrows indicate the motion of the footwall. Indicated are the 0 and 50 km slab depth contours of Gudmundsson and Sambridge (1998). Yellow curve is the trench axis determined by Curray (2005).

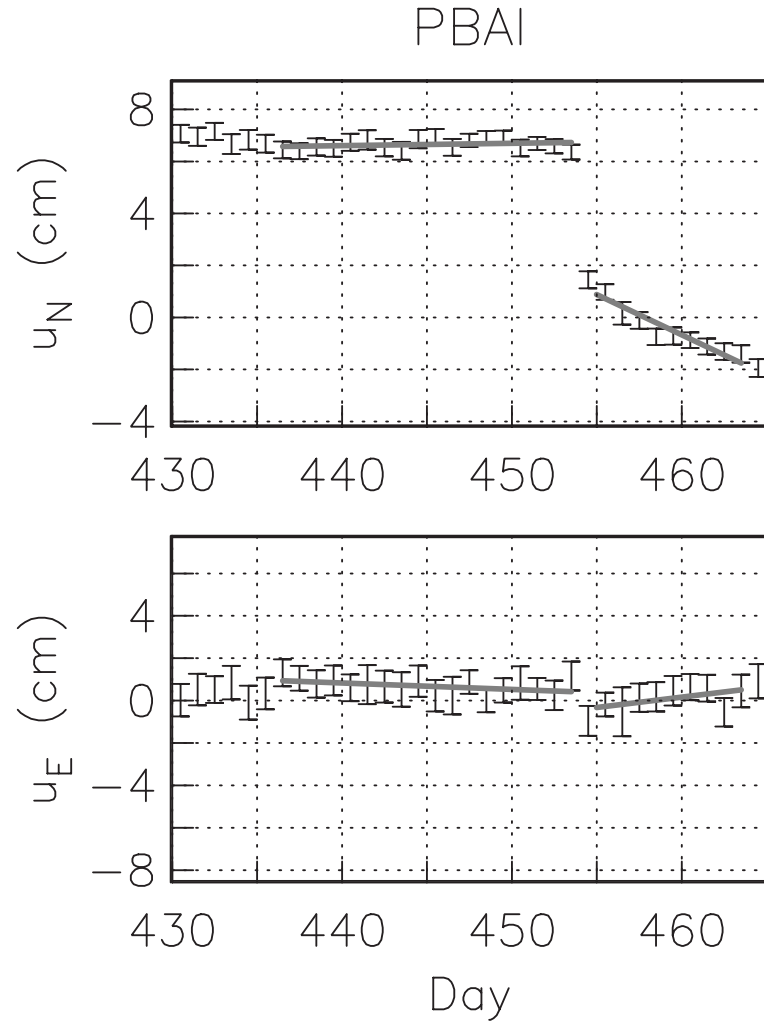


Figure 9: Observed GPS time series following the 28 March 2005 earthquake with $1\text{-}\sigma$ errors at GPS site PBAI. u_E and u_N refer to east- and northward displacement, respectively. Day numbers refer to the year 2004. Superimposed in thick gray are the straight-line fits to the 18-day portions of the pre-seismic and 7-day portions of the post-seismic time series.

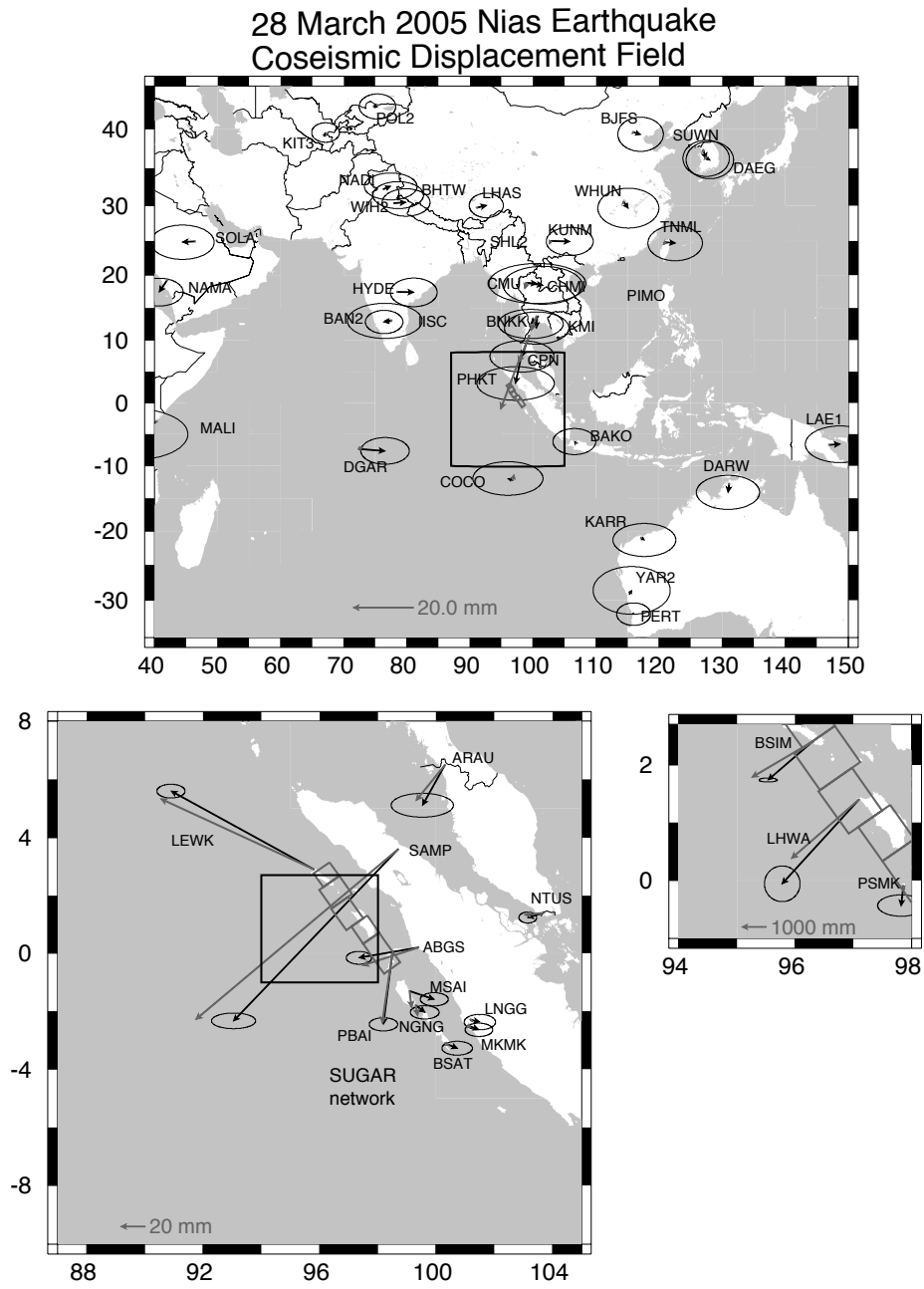


Figure 10: Coseismic horizontal displacement field of the 28 March 2005 earthquake, shown by black vectors with 95% error ellipses. Superimposed red vectors are the predicted static displacements on the PREM model using the 5-plane slip model given in Table 3. Gray lines indicate the fault planes.

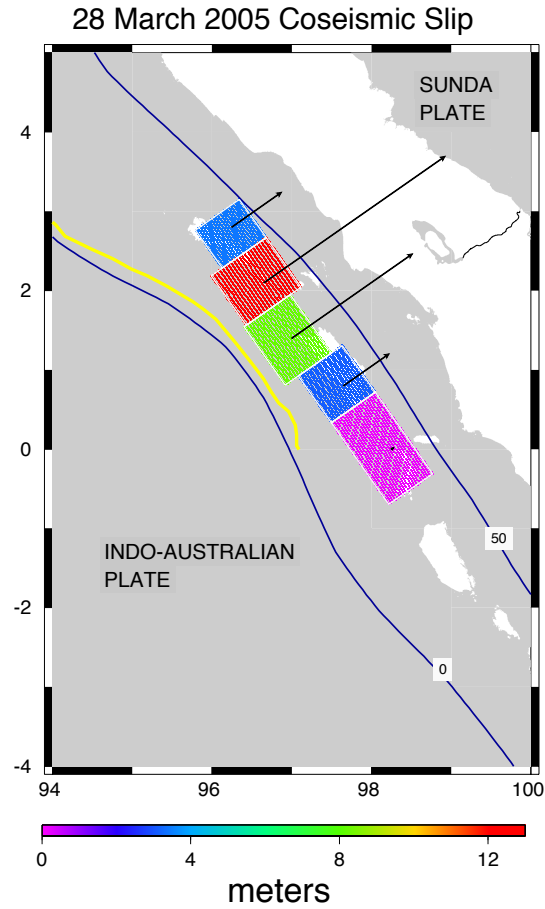


Figure 11: Coseismic slip of the Nias earthquake from inversion of the continuous GPS dataset. Arrows indicate the motion of the footwall. Indicated are the 0 and 50 km slab depth contours of Gudmundsson and Sambridge (1998). Yellow curve is the trench axis determined by Curray (2005).

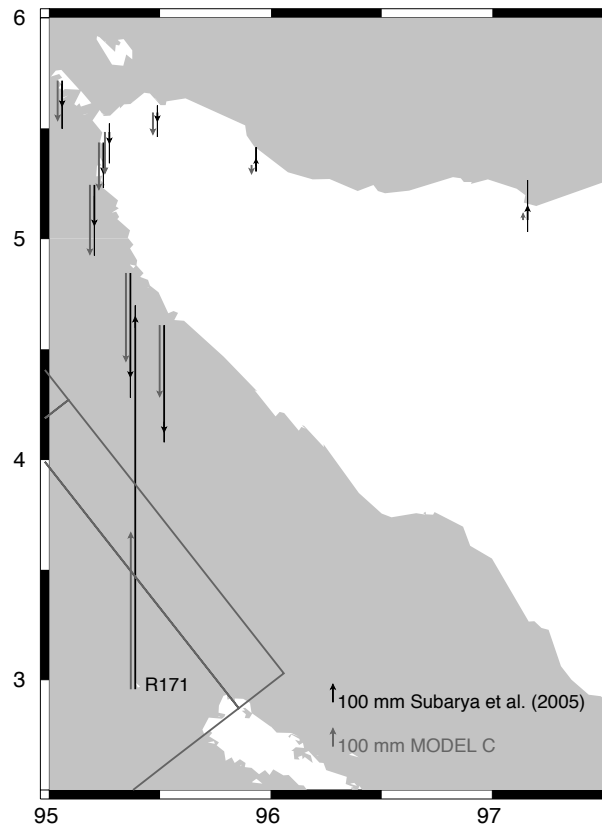


Figure 12: Predicted uplift on Sumatra-Andaman coseismic Model C around northern Sumatra compared with vertical campaign-GPS displacements (Subarya et al., 2006). Gray lines indicate the fault planes used to obtain Model C.

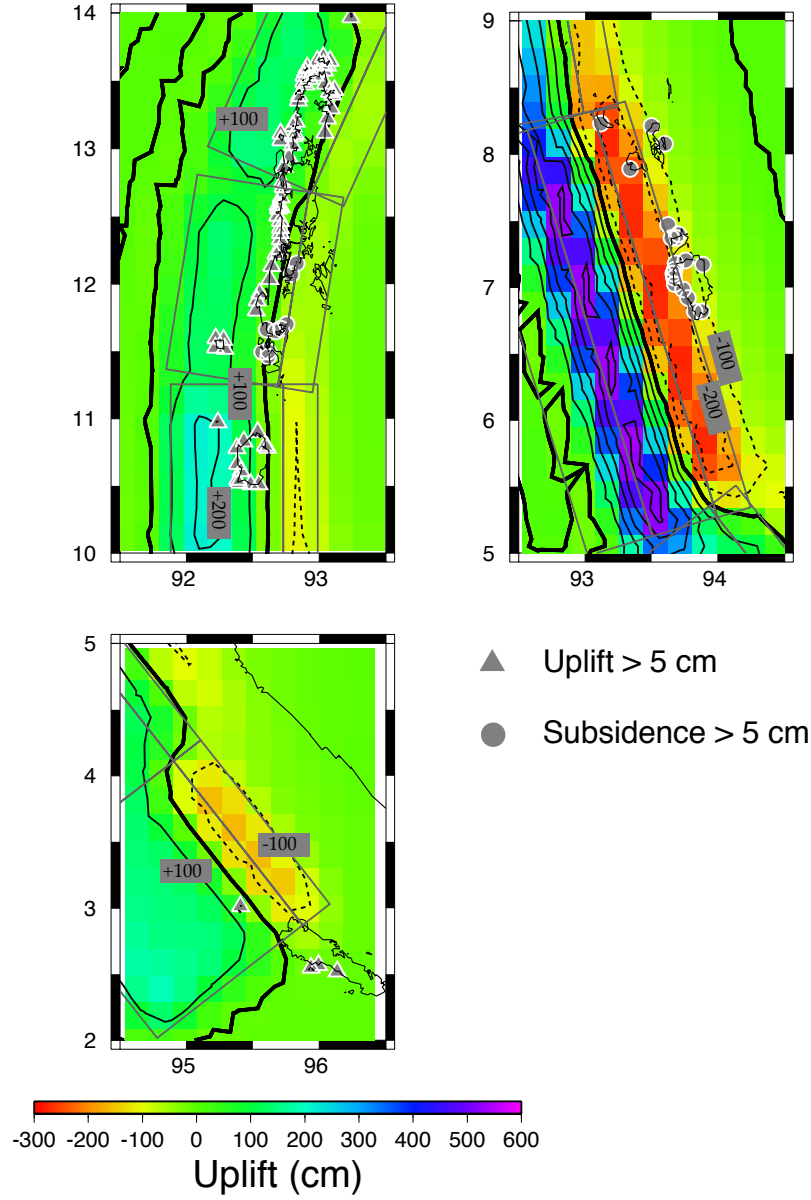


Figure 13: Predicted uplift on Sumatra-Andaman coseismic Model C. Thick black lines denote zero uplift contour. Superimposed are locations of uplift (triangles) and subsidence (open circles) determined by Meltzner et al. (2006) with either 5 cm minimum uplift or 5 cm minimum subsidence. Gray lines indicate the fault planes used to obtain Model C.

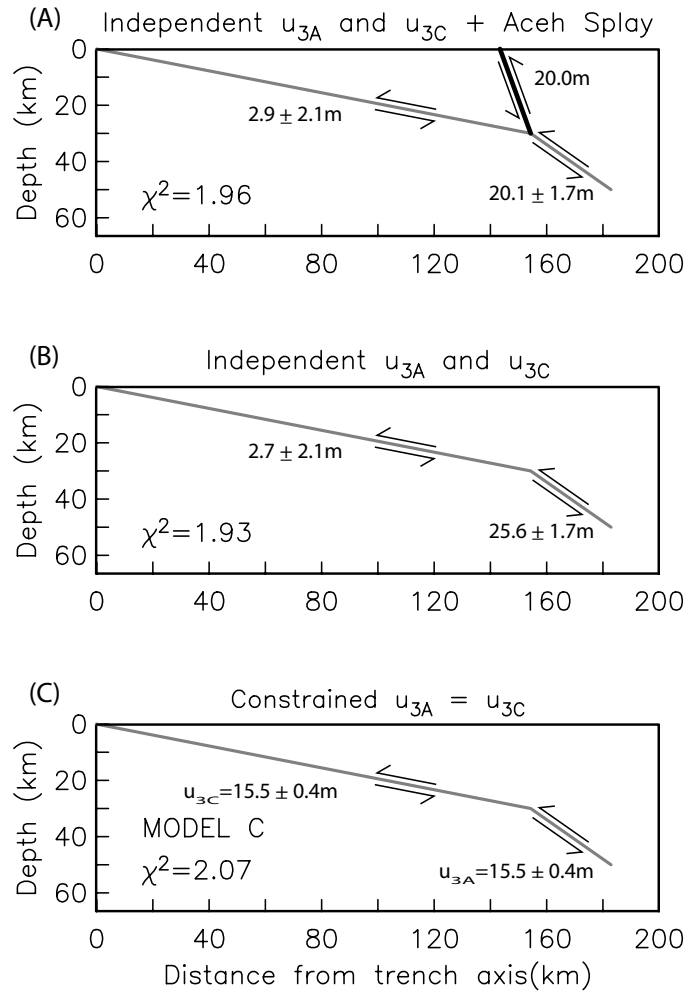


Figure 14: Estimated slip resulting from geodetic data inversions using variations of the preferred Model C. Case (a) uses a combination of independent dip slip on segments 3A and 3C and a dip slip of 20m prescribed on the Aceh splay. Case (b) allows for independent dip slip on segments 3A and 3C without the Aceh splay. Case (c) is Model C, which constrains the dip slip of segments 3A and 3C to be identical.

Segment	Endpoint [§]	d_1^\dagger km	d_2^\ddagger km	Rake	Length km	Width km	Strike* °	Dip °
1A	13.93°N 93.90°E	50	30	$\lambda_1 + 34^\circ$	162.5	34.9	24	35
1B	12.65°N 93.20°E	50	30	$\lambda_1 + 17^\circ$	162.5	34.9	7	35
1C	11.26°N 92.99°E	50	30	$\lambda_1 + 10^\circ$	162.5	34.9	0	35
1D	9.79°N 92.99°E	50	30	λ_1	162.5	34.9	350	35
1E	14.01°N 93.55°E	30	0	$\lambda_1 + 34^\circ$	162.5	97.1	24	18
1F	12.68°N 92.92°E	30	0	$\lambda_1 + 17^\circ$	162.5	97.1	9	18
1G	11.26°N 92.73°E	30	0	$\lambda_1 + 10^\circ$	162.5	97.1	0	18
1H	9.75°N 92.73°E	30	0	λ_1	162.5	97.1	350	18
2A	8.40°N 93.30°E	50	30	λ_{2A}	355	34.9	343	35
2B	8.33°N 93.05°E	30	15	λ_{2B}	355	58.0	343	15
2C	8.18°N 92.56°E	15	0	λ_{2C}	355	58.0	343	15
3A	5.51°N 94.13°E	50	30	λ_3	175	34.9	322	35
3B	4.27°N 95.11°E	50	30	λ_3	175	34.9	322	35
3C	5.35°N 93.93°E	30	0	λ_3	175	157.2	322	11
3D	4.11°N 94.90°E	30	0	λ_3	175	157.2	322	11

Variable rake is specified on the Andaman (segment 1) subsegments of variable strike such that absolute slip direction is kept constant. For a subsegment with strike ϕ and dip δ , the rake λ theoretically obeys the relationship

$\phi - 350^\circ = \tan^{-1}(\tan \lambda \cos \delta) - \xi$, where ξ is the azimuth of the slip direction.

For simplicity we adopt the approximation $\phi - 350^\circ = \lambda - \lambda_1$.

[§] Latitude and longitude of northernmost point on lower edge.

[†] Lower fault edge depth; [‡] Upper fault edge depth.

* Segment strike in degrees clockwise from due North.

Table 1: Fault geometry parameters of coseismic rupture planes

Model	u_{1D} m	u_{1E} m	u_{1F} m	u_{1G} m	u_{1H} m	u_{2B} m	λ_{2B} °
A [‡]	0.5 ±0.5	6.6 ±0.2	5.6 ±0.3	8.0 ±0.4	16.2 ±0.5	16.2±0.3	114±2
B	0.0 ±0.5	6.4 ±0.2	5.3 ±0.3	7.4 ±0.4	16.4 ±0.5	0.0 [†]	—
C (Preferred)	2.3 ±0.5	6.6 ±0.2	5.2 ±0.3	7.8 ±0.4	16.6 ±0.5	19.4 ±0.4	110 ±2

Model	u_{2C} m	λ_{2C} °	u_{3A} m	u_{3B} m	u_{3C} m
A [‡]	16.2 ±0.3	114 ±2	14.7 ±0.4	1.0 ±0.6	14.7 ±0.4
B	56.8 ±2.0	120 ±2	16.2 ±0.4	3.6 ±0.7	16.2 ±0.4
C (Preferred)	0.0 [†]	—	15.5±0.4	-0.5 ±0.6	15.5 ±0.4

Model	u_{3D} m	$\chi^{2\S}$
A [‡]	9.2 ±0.3	2.32
B	9.1 ±0.3	4.40
C (Preferred)	9.2 ±0.3	2.07

u_i and λ_i denote, respectively, slip and rake on fault i .

We hold fixed $\lambda_1 = 105^\circ$ and $\lambda_3 = 90^\circ$.

Variable rake on Andaman subsegments is described in Table 1.

[§] Reduced χ^2 , equal to the full χ^2 divided by $N - n$, where $N = 316$ is the number of data constraints and n is the number of independent parameters ($n = 10$ for all models).

The slip of subsegments 3A and 3C are constrained to be equal in all inversions.

[†] Value fixed in inversion

[‡] Constrained such that plane-2B and plane-2C slips and rakes are equal.

Table 2: Inverted slip parameters of 26 December 2004 earthquake

Segment	Endpoint [§]	d_1^\dagger km	d_2^\ddagger km	Length km	Width km	Strike* °	Dip °	Slip m	Rake °
1	3.15°N 96.34°E	42	22	65	77.3	325	15	0.3±0.05	90.0
2	2.67°N 96.68°E	42	17	85	96.6	325	15	12.3±0.3	97±0.4
3	1.95°N 96.98°E	30	9	100	81.1	325	15	8.2±0.6	91±4
4	1.31°N 97.63°E	42	22	80	77.3	325	15	3.1±0.5	107±3
5	0.72°N 98.05°E	42	22	140	77.3	325	15	0.2±0.02	119±15

[§] Latitude and longitude of northernmost point on lower edge.

[†] Lower fault edge depth; [‡] Upper fault edge depth.

* Segment strike in degrees clockwise from due North.

Table 3: Fault-plane and inverted-slip parameters of 28 March 2005 Nias earthquake